Lawrence Berkeley National Laboratory

Title

Integrated Experimental and Modeling Study of Geochemical Reactions of Simple Fracturing Fluids with Caney Shale

Permalink

https://escholarship.org/uc/item/740190qf

Journal

Energy & Fuels, 36(17)

ISSN

0887-0624

Authors

Awejori, Gabriel Adua
Doughty, Christine
Xiong, Fengyang
et al.

Publication Date

2022-09-01

DOI

10.1021/acs.energyfuels.2c01739

Copyright Information

Peer reviewed

1 **Integrated Experimental and Modeling Study of Geochemical Reactions of Simple**

2 **Fracturing Fluids with Caney Shale**

3 Gabriel Adua Awejori[1], Christine Doughty[2], Fengyang Xiong[1], Thomas Paronish[3], Nicolas

4 Spycher[2], Mileva Radonjic[1,4,*]

5

6 [1]Hydraulic Barrier Material and Geomimicry Laboratory, School of Chemical Engineering, Oklahoma State

7 University, 420 Engineering North, Stillwater, OK 74078, USA

8 [2]Energy Geosciences Division, Lawrence Berkeley National Laboratory, 1 Cyclotron Road, Berkeley, CA 94720,

9 USA

10 [3]Leidos Research Support Team, National Energy Technology Laboratory, 3610 Collins Ferry Road, Morgantown,

11 WV 26505, USA

12 [4]Boone Pickens School of Geology, Oklahoma State University, 105 Noble Research Center, Stillwater, OK 74078,

13 USA

14 *Corresponding author: Mileva Radonjic. Mileva.radonjic@okstate.edu

15

16 **Abstract**

17 Interactions between rock minerals and hydraulic fluids directly impact the geochemical

18 and geomechanical properties of shale formations. However, the mechanisms of geochemical

19 reactions in shale unconventional reservoirs remain poorly understood.

20 To investigate the geochemical reactions between shale and hydraulic fracturing fluids, a

21 series of batch reactor experiments were undertaken. Three rock samples with different

22 mineralogical compositions and three fluid samples of different compositions (deionized water,

23 deionized water + 2% potassium chloride (KCl), and deionized water + 0.5% choline chloride

24 ($C_5H_{14}ClNO$) were used.   Experiments were undertaken at reservoir temperature and

25 atmospheric pressure. Elemental compositions of effluents after 1, 3, 7, 14, 28 days were

26 analyzed using Inductively Couple Plasma Mass Spectrometry (ICP-MS). Medical Computed

27 Tomography (CT) scan and X-ray Fluorescence (XRF) were conducted on the entire core run to

28 help upscale results obtained from rock-fluid interaction experiments. Geochemical modeling

29 using a reactive simulator, TOUGHREACT, was undertaken to corroborate experimental results.

30 Results show that lower pH triggered high dissolution rates in the rock samples,

31 especially the carbonate components. As pH increased, the rate of dissolution declined

32 significantly, though for most cases dissolution still continued. Observed dissolved silica

1

concentrations were much higher than the quartz solubility, suggesting that much of the silica originates from more soluble silica polymorphs and possibly desorption from clay mineral exchange sites. Concentration of most elemental species in solution increased but aluminium and magnesium concentrations declined rapidly following initial entry into solution. Geochemical modeling corroborated the conclusions regarding mineral dissolution and precipitation observed from experiments, notably; the dissolution of calcite and oxidation of pyrite in reacted shale samples, the likely presence of silica polymorphs such as opal, chalcedony or amorphous silica in these samples, and the reduction of Al and Mg concentrations in solution by precipitation of secondary aluminosilicate phases.

The de-flocculation of clay minerals during reaction implies fines migration after hydraulic fracturing. This is detrimental to reservoir productivity as clay fines are displaces and lodged within the micro and nano-fractures created during fracturing. The immediate consumption of aluminium and magnesium also has implications on blockage of hydrocarbon pathways due to precipitation of new minerals in these locations.

Key words: Caney Shale, Hydraulic fracturing, Rock-fluid interaction, Geochemical reactions, Geochemical modeling

1. Introduction

The Caney Shale is a largely unexploited but potentially economically viable unconventional petroleum formation found within the South-Central Oklahoma Oil Province (SCOOP) [1–4]. This formation has largely been regarded as a source and seal formation, accounting for its present relatively unexploited status [2,3,5,6]. The target for most drilling in the area has been the Woodford Shale which is directly overlain by the Caney Shale. Though the Caney Shale is replete with recoverable hydrocarbon resources, little research and exploration activity has been undertaken in this formation. Mechanisms of interactions between formation and hydraulic fracturing fluids for this formation are therefore less known than for extensively exploited shales such as the Barnett and the Marcellus [7–10].

61   From points of deposition through diagenesis and other lithification processes, formation

62   rocks and fluids undergo a series of reactions until they attain thermodynamic equilibrium or a

63   chemical (near-) steady state at their present locations within the subsurface. Any changes in the

64   conditions of this equilibrium triggers instability which leads to reactions. During hydraulic

65   fracturing, the introduction of fracturing fluids of different chemical compositions into the

66   formation triggers reactions between the formation and injected fluids [11,12]. These reactions lead

67   to dissolution of minerals and precipitation of new minerals, which have implications on the

68   petrophysical properties of the reservoir [13]. Dissolution of minerals may lead to increased

69   porosity and permeability but can also lead to a weakened matrix that may collapse under

70   confining pressures, thus reversing the gained porosity and permeability. This is common in

71   carbonate-rich formations where carbonate dissolves under low pH conditions. Precipitation of

72   new minerals may however lead to reduced porosity and permeability as these normally grow

73   within flow pathways.

74   The most common and problematic reactions within the subsurface are those between

75   injected fracturing fluids and clay minerals within the formation. Most clay minerals tend to react

76   with fracturing fluids because the major component of most fracturing fluids is water [14]. Clay

77   swelling is primarily the result of adsorption of cations and fluids on the surface or absorption

78   into the inter-layer structure of clay minerals. The main driver of this process is the

79   electrochemical interactions between clay minerals and surrounding fluids. The nature, quantity,

80   and charges of cations within the clay interlayer determine the level and type of swelling that

81   occurs. Formation damage through clay swelling in the context of enhanced oil and gas recovery

82   has been dealt with extensively [15,16].

83   Crystalline and osmotic swelling of clay minerals have been identified as the two main

84   types of swelling mechanisms in clay minerals [14,17]. Crystalline swelling, also referred to as

85   surface hydration, occurs when water molecules are adsorbed onto the negatively charged

86   surfaces of clay platelets and held in place by hydrogen bonding. Subsequent layers of water

87   molecules are then aligned on top of the first layer, forming a quasi-crystalline structure between

88   unit clays. Osmotic swelling, on the other hand, occurs when water is osmotically drawn into the

89   interlayer space of clay units due to disequilibrium in cationic concentrations between

90   surrounding fluid and clay inter-layer. This increases the c-spacing (inter-layer width) of the clay

3

91   unit. Osmotic swelling causes greater swelling than crystalline swelling and has been identified

92   as the most problematic swelling responsible for loss of porosity and permeability during drilling

93   and hydraulic fracturing operations [18].

94   Another issue is fines migration, which is prevalent in illite/smectite mixed layer clays,

95   creates more problems in producing formations than clay swelling. Illite/Smectite mixed layer

96   clays are predominant in most unconventional shale reservoirs in North America. Dislodged fine

97   particles are transported and deposited along pore throats, which cause significant losses in

98   permeability and inhibit fluid flow (Dawuda and Srinivasan, 2022).   Fines migration is caused

99   by both chemical and mechanical processes. In the chemical process, the adsorption and

100   absorption of cations to clay surfaces and interlayers reduces and eventually eliminates the

101   electrostatic forces that hold the clay platelets and clay layers together, thus causing de-

102   flocculation of the clay platelets or disintegration of clay layers and subsequent migration as fines

103   [19–21]. Mechanical destabilization and transport of fines occur when the mechanical forces due to

104   moving fluids overcome the adhesive forces holding fines to formation walls, thus dislodging and

105   transporting these fines.

106   In hydraulic fracturing fluid preparation, clay stabilizers are crucial components added to

107   counter swelling of clays and migration of fines during hydraulic fracturing. Concerted efforts

108   have thus been made to investigating different types of clay stabilizers as well as mechanisms

109   under which they function best. Consequently, there are several clay stabilizing additives

110   currently used in industry. Two of the most common types of temporary clay stabilizers used in

111   industry are potassium chloride (KCl) and choline chloride ($C_5H_{14}ClNO$). KCl inhibits clay

112   swelling by exchanging potassium cations with sodium, magnesium, and other cations on clay

113   surface or interlayer. These adsorb on the clay surface or form a 'double layer', thus preventing

114   further interaction with water to cause fines migration.   Also, the potassium cations are

115   exchanged for cations in the clay interlayer, which locks the interlayer and prevents further

116   interactions with water that may cause swelling. $C_5H_{14}ClNO$, on the other hand, works by

117   attaching itself to clay surfaces and preventing interactions with water by repelling water

118   molecules with its hydrophobic tail. Due to the mechanisms described above, these clay

119   stabilizers are able to prevent clay swelling and fines migration.

4

120   This work is aimed at assessing the reactions between formation rocks and fracturing

121   fluids containing KCl or $C_5H_{14}ClNO$ clay stabilizers. Deionised (DI) water is used as a baseline

122   fluid in these experiments. The key factors governing these reactions are assessed to provide

123   insights on expected reaction products for various rock and fluid compositions. This research

124   also provides data on the efficiency of temporary clay stabilizers and on element concentrations

125   in flow back waters for various rock compositions.

126   The main objective of this study is to assess the effects of KCl and $C_5H_{14}ClNO$ in

127   inhibiting adverse clay-fluid interactions. To achieve this, rocks of different mineralogical

128   compositions were selected at different depths in the Caney Shale, crushed, ground, and reacted

129   with simple fracturing fluids as well as deionized water under temperature conditions mimicking

130   the reservoir environment and at atmospheric pressure. X-ray Diffraction (XRD) analysis and

131   Inductively Couple Plasma Mass Spectrometry (ICP-MS) were used to measure mineralogical

132   compositions and elemental concentrations in fluids, respectively. Medical Computed

133   Tomography (CT) scan and X-ray Fluorescence (XRF) were also conducted on the entire core

134   run to help upscale results obtained from rock-fluid interaction experiments.

135   This study was carried out in two phases: laboratory experiments phase and a simulation/

136   modeling phase. In the experimental phase, batch reactor experiments were run for 28 days under

137   laboratory conditions designed to mimic down-hole shut-in periods when most of the rock-fluid

138   interactions occur. The simulation phase of this work involved numerical modeling of the rock-

139   fluid interactions occurring during the batch reactor experiments conducted in the laboratory

140   experimental phase. The objective of the simulation phase was to predict and help interpret

141   laboratory experimental results.

142   **2.0 Materials and Methods**

143   **2.1 Experimental Design**

144   Batch reactor experiments are structured to mimic conditions in subsurface of the Caney

145   Shale during shut-in periods. In standard hydraulic fracturing treatment of wells, there are a few

146   days to several weeks of shut-in following completion of hydraulic fracturing treatments. During

147   this period, the hydraulic fracturing fluids in the formation react with rock minerals causing

148   dissolution and precipitation of new minerals. Following shut in, not all the fluids injected into

149   the formation are recovered. Therefore, reaction between formation and injected fluids continue.

150   For this study, the reaction time is 28 days [22], representing a typical shut-in period as
151 identified by Vidic et al., (2013) [22]. During this period, the reaction vessels are covered and
152 placed in an oven with pre-set specific conditions: temperature of 95 °C and atmospheric
153 pressure. Shale samples are crushed and ground to particle size range of 10 μm to 50 μm. This
154 exposes more surface area of the rock to react with the surrounding fluid. The initial liquid to
155 solid ratio for the experiment is 200 ml/g; 0.7 g of crushed rock reacted with 140 ml of various
156 simplified fracturing fluids.

157   Sampling of effluent occurs at predetermined intervals: 1, 3, 7, 14, 21, and 28 days
158 following the start of the experiment. During sampling, the reaction vessel is taken out of the
159 oven and a syringe is used to collect about 10 ml of effluent from the sample vessel. Sampled
160 effluents are sieved through a 0.22 μm filter and subsequently stored in a refrigerator pending
161 analyses. Each sampling event lasts about 10 minutes.

162 **2.2 Materials**

163   Samples used for experimental investigations include Caney Shales selected from
164 different depths from Caney well in South Central Oklahoma (Figs. 1 and 2). Analyses on the
165 rocks with XRD show variance in mineralogical compositions (Table 1). Though quartz is the
166 predominant mineral in all the samples, the differences in relative amounts of quartz, carbonate,
167 and clays are significant (Table 1). The reaction dynamics are therefore expected to be different.
168 Samples have been designated High Quartz (HQ), Moderate Quartz, Carbonate, and Clay (MQ),
169 and High Clay (HC), based on their relative mineralogical compositions.

170   Fluid samples used for experimental investigations are simplified hydraulic fracturing
171 fluids (Table 2). These include 2% KCl and 0.5% $C_5H_{14}ClNO$ both prepared in the laboratory
172 using deionized water as base fluid and set to pH of 4 by adding hydrochloric acid. DI water is
173 also used as a fluid in the experiments to serve as a control (Table 2). The relatively high clay
174 mineralogical composition of the Caney Shale served the main motivation for choosing temporal
175 clay stabilizers as the main components of simplified fracturing fluids. Properties of fluids used
176 in the experiment are presented in Table 2.

177 **2.3   Analytical Methods**

6

178   The main analytical methods adopted in the experimental phase of this study include
179   XRD for estimating the mineralogical composition of rock samples, ICP-MS for measuring the
180   elemental concentrations in effluents, and medical CT scan and XRF employed to study the
181   entire length of drilled core in order to help upscale results obtained from the main analyses.

182   The following details how each analysis was undertaken:

183   XRD analyses were performed on rock powder samples before the beginning of the
184   experiments to assess their mineralogical compositions. This was achieved with a Bruker D8
185   advance X-Ray Diffractometer with Lynxeye detector. Scanning was run from 5 to 80 degrees 2-
186   theta angle with a 0.01 degree step and dwell time of 0.5 seconds. Semi-quantitative analyses
187   were also accomplished with the BRUKER's Diffrac.suite eva.

188   To measure the elemental concentrations in effluents, the extracted fluids were first
189   sampled through a 0.22 μm filter after extraction from the reaction vessel. An Oakton pH 150
190   meter was used to measure pH of the fluid immediately after sampling. Sampled fluids were
191   subsequently stored at temperatures of about 4 ºC. Samples were acidified to ensure all the
192   elements are in solution before analyses using ICP-MS for elemental concentrations of major
193   elements. The elements tested included, Na, Ca, Mg, K, S, B, Si, Al, Fe, and Mn. At the end of
194   experiment period, excess effluents were poured into plastic bottles and stored in a refrigerator.

195   The entire core run was sent to the National Energy Technology Laboratory (NETL) in
196   Morgantown, WV for XRF and medical CT scans [23]. The Medical Toshiba® Aquilion TSX-
197   101A/R medical scanner was used for the acquisition of medical CT scans at voxel resolutions of
198   0.43 x 0.43 mm in the XY plane and 0.5 mm in the core axis. For the purpose of this research,
199   3D volumes obtained from scans were re-sliced along the longitudinal axis and used as an image
200   log. Images are observed to transition from dark to brighter scales. Totally dark regions in the
201   scan represent areas of low density such as air, whereas brighter areas are associated with regions
202   of high-density minerals such as pyrite.

203   The portable handheld Innov-X® X-Ray Fluorescence Spectrometer was used for XRF
204   analysis, aimed at measuring relative elemental abundances throughout the well. Also, the
205   Mining-Plus suite was run at 6 cm resolution for 60 seconds of exposure time per beam through
206   the entire 650 feet of core. The Mining-Plus suite utilizes a two-beam analysis to report the
207   fractional elemental abundances relative to the total elemental composition (i.e. out of 100%),

7

208   and resolve major (Mg, Al, Si, P, S, Cl, Fe, K, Ca, Ti), minor (V, Cu, Ni, Cr, Mn, Pb), trace

209   elements, and an aggregated "light element" (H to Na). The data is filtered for errors exceeding

210   20% of the measured data [24].

2.4 Numerical Model Development

212   Based on the description of the experiment and the data provided above, simple

213   geochemical models of the batch reactor experiments were constructed for the HC material in

214   KCl fluids and modeled with the reactive transport simulator TOUGHREACT [25,26]. A simple

215   "batch" problem was modeled in which there is no fluid flow or chemical transport, and

216   temperature is held constant at 95 ºC as in the experiments. Cation exchange and aqueous

217   complexation (including redox) were modeled at thermodynamic equilibrium while mineral

218   dissolution and precipitation were modeled to proceed under kinetic constraints.

219   Initial simulations (referred to as Model 1) ignored the presence of headspace (primarily

220   air, with some water vapor) above the fluid in the beaker, and did not consider the introduction of

221   atmospheric O_2 into the beaker during sampling. Also, the presence of amorphous Si (modeled as

222   opal-CT) and organic matter (modeled as graphite) in the sediment were not considered. More

223   refined simulations (referred to as Model 2) including these phases as well as headspace and air

224   contamination during sampling were later conducted with better results.

225   The data available for modeling were limited, so a number of assumptions were made.

226   Therefore, results shown here should be viewed as more qualitative than quantitative, and

227   illustrative of the geochemical processes modeled and modeling capabilities. A more complete

228   geochemical and physical characterization of the samples would be necessary to better constrain

229   the model results, including but not limited to parameters such as grain size distribution, cation

230   exchange capacity and surface area, clay mineralogy and composition, as well as redox

231   conditions.

232   In both Model 1 and Model 2, a single grid block represents the reaction beaker, which is

233   held at constant pressure and temperature. In both cases, the withdrawal of liquid samples from

234   the beaker at prescribed time intervals (1, 3, 7, 14, 21, 28 days), and the accompanying decrease

235   in liquid to solid ratio, was modeled explicitly by withdrawing a finite amount of solution (10

236   ml) from the reaction grid block over a 1-minute time interval at each sampling event. In doing

237   so, the effect of increasing solid/liquid ratio due to the withdrawal of fluid samples was modeled

238   as it affects the reactive surface areas of minerals considered in the simulations.

239   In Model 1, the reaction beaker is simulated as a fully liquid-saturated grid block with

240   elasticity to allow for sample withdrawal without affecting pressure. In Model 2, the reaction

241   beaker is modeled as a fixed-volume, partially liquid-saturated grid block to allow for a

242   headspace. In both models, the beaker grid block was given the volume of the experimental

243   beaker and proportions of solution, shale (and head space in Model 2) consistent with the

244   experimental setup.

245   A second grid block connected to the grid block representing the beaker was added to

246   Model 2, to simulate the presence of atmosphere above the beaker. The atmospheric grid-block

247   was given an infinite volume and set with zero liquid saturation, thus with only gas present. The

248   withdrawal of liquid samples from the beaker causes atmosphere to be drawn into the beaker grid

249   block, as happens in the experiments. The atmosphere drawn into the beaker was given an

250   atmospheric CO_2 concentration and O_2 concentrations calibrated to best match results of

251   experiments. Therefore, the modeled oxygen influx was controlled by the sample withdrawal rate

252   and calibrated O_2 concentration in the air influx, thus effectively approximating oxidation under

253   some kinetic constraints.

254   The primary aqueous species considered in both models were H^+, H_2O, Na^+, K^+, Ca^{2+}, Mg^{2+}, Fe^{2+},

255   Al^{3+}, Cl^-, $SiO_2(aq)$, HCO_3^-, HS^-, and SO_4^{2-}. The minerals included in the simulations are shown in

256   Table 3. Gases representing contact with air include O_2 and CO_2. N_2 was omitted because it is

257   non-reactive. A critical parameter in these simulations is the specific surface area of the

258   minerals, which controls chemical reaction rates and is derived from particle size and

259   assumptions about close packing of particles. For the present study, particle size is not well

260   known and was adjusted to yield the most reasonable model match to experimental data. For

261   Model 1, a uniform grain size for all minerals was assumed (3 μm), whereas the grain size was

262   further adjusted for different groups of minerals in Model 2 (20 μm for carbonates and quartz, 1

263   μm for other minerals).

264   **3.0 Results**

9

265   Elemental concentrations in effluents are assessed to understand mineral
266 dissolution/precipitation and impacts of clay stabilizers during reactions. This first part of this
267 work compares the influence of fluid versus rock composition on the reaction path. Two sets of
268 plots are employed; the first set shows effluent chemistry due to impact of fluid composition
269 whiles the second set shows impact of rock composition. This comparison helps to understand
270 the crucial variables controlling subsurface rock-fluid interactions within Caney Shale.

271   In a second part of this work, the rate of effluent chemistry changes with time is
272 evaluated. This helps explain key mechanisms of dissolution, precipitation and de-flocculation in
273 reservoir. Effluent evolution is modeled and compared to experimental results to understand the
274 long term implications of rock-fluid interactions in the subsurface. Finally, results of experiments
275 and models are up-scaled based on CT scan and XRF elemental composition of 650 ft recovered
276 core.

277 **3.1   Effluent Analysis: pH Trend as a Function of Rock and Fluid Compositions**

278 Results show a rapid increase in pH values for KCl and $C_5H_{14}ClNO$ fluids on the first day,
279 considering these fluids were set to a pH of 4.0 at the beginning of the experiment (Figs. 3a and
280 3b). pH values from both sets of graphs show that samples with deionized water (DI) and
281 $C_5H_{14}ClNO$ exhibit stable pH values for the first two weeks followed by steep rise in pH for one
282 week and then another stabilization during the third week. With the KCl fluid however, the pH
283 increases steadily and only within the first week.

284   The initially low pH values for KCl and $C_5H_{14}ClNO$ fluids caused rapid dissolution of
285 carbonate minerals in both fluids, which subsequently serve as a strong pH buffer. Initial rapid
286 pH increases in KCl relative to $C_5H_{14}ClNO$ may be due to early stabilization of clay in the
287 former, thus allowing a faster dissolution reaction with carbonates to increase the pH. The action
288 of clay minerals in suppressing the dissolution of carbonates is countered once clay minerals are
289 stabilized. Fig. 3a and 3b show plots of pH as a function of fluid composition (Fig. 3a) and pH as
290 a function of rock composition (Fig. 3b).

291   **3.2   Effluent Analysis: Calcium (Ca) Element Concentration as a Function of**
292 **Rock and Fluid Compositions**

293   The dissolved Ca concentration is consistently the highest in effluents of KCl, followed
294 by $C_5H_{14}ClNO$ and DI water (Figs. 4a and 4b). The Ca concentration increases throughout the

10

295 experiment for all the rock and fluids samples. Though slight initially, Ca concentration in the

296 MQ sample is the highest, followed by HQ with HC showing least concentrations. There is

297 however a lag in Ca concentration in MQ sample to HQ sample for KCl fluid on days 1 and 3.

298 Disparity in elemental fluid concentrations increases with time for all rock samples. Trends show

299 Ca concentration in solution is mainly influenced by the fluid composition.

300   High dissolved Ca concentrations in the effluents of KCl and $C_5H_{14}ClNO$ are the result of

301 higher dissolution of carbonate minerals due to the initial low pH set for these fluids. The higher

302 dissolved Ca concentrations in the HQ sample, relative to HC samples, despite the latter having a

303 higher carbonate mineral composition, may be explained by the suppression of carbonate

304 dissolution due to presence and interference of clay minerals. Adsorption of Ca cations released

305 into solution at clay surfaces is one way Ca concentration is reduced in effluent. This is further

306 confirmed by the initial higher concentrations of Ca in HQ relative to MQ samples (which have

307 the highest carbonate composition) due to the latter's high clay content. The subsequent rise in

308 Ca ion concentration in the latter is thought to occur after stabilization of clay mineral

309 constituents of the sample.

310   Fig. 4 shows plots of Ca concentration as a function of fluid composition (Fig. 4a) and Ca

311 concentration as a function of rock composition (Fig. 2b).

312

313 **3.3   Effluent Analysis: Silicon (Si) Element Concentration as a Function of Rock and**
314 **Fluid Compositions**

315   Dissolved Si concentrations remain highest in KCl solutions for all samples throughout

316 the experiments (Fig. 5a). With different rock types, the dissolved Si concentration in samples

317 with KCl levels off after day 10 (Fig. 5b). In contrast, concentrations in DI water and

318 $C_5H_{14}ClNO$ solutions show continuous increment for the duration of the experiment, though with

319 lower concentrations than KCl. The concentration of Si in $C_5H_{14}ClNO$ does not level-off but

320 continues to increase at the latter stages of the experiment, and may be projected to pass the

321 concentrations observed in the KCl.

322   Dissolved Si concentration largely exceed quartz solubility, thus may result from more

323 soluble (possibly biogenic) silica (SiO_2) polymorphs and Si imbedded in clay minerals. The lag

324 in Si concentration increase in $C_5H_{14}ClNO$ relative to KCl and the former's upward surge during

11

325 the final part of the experiment is suggestive of the speed with which each fluid is able to

326 stabilize clay minerals thus allowing for dissolution of silica. Fig. 5 shows plots of Si

327 concentration as a function of fluid composition (Fig. 5a) and Si concentration as a function of

328 rock composition (Fig. 5b).

3.4 Effluent Analysis: Aluminium (Al) Element Concentration as a Function of Rock and Fluid Compositions

331 The dissolved Al concentrations show a continuous downward trajectory for all samples,

332 though there is a small increase in Al concentration in DI water after day twenty-one (21) (Fig.

333 6a). The Al concentration is higher in DI water and $C_5H_{14}ClNO$ solutions, whereas the samples

334 with KCl show almost no Al after day three (3) (Fig. 6b). The disparities between the graphs

335 reveal that Al concentration is highly dependent on the fluid composition.

336 Though KCl and $C_5H_{14}ClNO$ are meant to stabilize clays, the initially lower pH of these

337 fluids leads to rapid reactions with clay minerals releasing Al into solution. Albite and muscovite

338 dissolution at lower pH values may also contribute to Al concentration in the fluid. The rapid

339 downward trajectory of Al concentration suggests rapid precipitation of secondary Al phases.

340 Also, Al can rapidly exchange on clay surfaces by monovalent and divalent cations, but once

341 these are released into solution, they tend to react with other ions in solution to form precipitates

342 or colloids.

343 Fig. 6 shows plots of Al concentration as a function of fluid composition (Fig. 6a) Al

344 concentration as a function of rock composition (Fig. 6).

3.5 Effluent Analysis: Sulfate Concentration as a Function of Rock and Fluid Compositions

347 The concentration of SO_4^{2-} is high for KCl in samples HQ and MQ whilst concentration in

348 sample HC is about the same for all the solutions (Fig. 7a). The SO_4^{2-} concentration trend begins

349 to flatten after 14 days. The concentration of SO_4^{2-} in HQ and MQ samples are consistently higher

350 than in sample HC (Fig. 7b). From the foregoing, concentrations of SO_4^{2-} can be said to be

351 dependent to equal extent on both the fluid type and rock type.

352 High concentrations of SO_4^{2-} in HQ and MQ samples suggests the dissolution of pyrite.

353 The relatively low SO_4^{2-} concentration in sample HC may imply pyrite dissolution in this sample

354 is hampered by the high clay contents. The steady rise in SO_4^{2-} concentration suggests that little

12

355   or no precipitation of secondary SO_4^{2-} minerals occurs during the period of the experiment. Fe

356   generated from pyrite dissolution is not detected, presumably because of oxidation upon

357   sampling (resulting in the precipitation of Fe (III) oxy-hydroxides such as goethite, as suggested

358   by modeling results). Iron oxide precipitation has been observed in other studies (Pearce et al.,

359   2018)

360   Fig. 7 shows plots of SO_4^{2-} concentration as a function of fluid composition (Fig. 7a) SO_4^{2-}

361   concentration as a function of rock composition (Fig. 7b).

362 **3.6 Effluent Analysis: Boron (B) Element Concentration as a Function of Rock and Fluid**
363 **Compositions**

364   The dissolved B concentrations are consistently and progressively higher in KCl

365   solutions, then begin to flatten after 21 days (Fig. 8a and 8b). In contrast, B concentrations are

366   lower and of similar magnitude in DI and $C_5H_{14}ClNO$ solutions, and display increasing trends

367   that do not appear to flatten over the length of the experiment. Fluid type therefore has a greater

368   influence in the amount of B that enters into solution.

369   Initial rock analysis by XRD did not identify B bearing minerals in the rock samples. B in

370   aqueous fluid may thus have come from desorption in clay sites. B has been reported to be

371   capable of being adsorbed on clays with disequilibrium capable of causing its release [27]. Higher

372   concentrations of B in KCl fluids may be due to the stabilization process of the clay minerals

373   which prevents re-adsorption of released B.

374   Fig. 8 shows plots of B concentration as a function of fluid composition (Fig. 8a) and B

375   concentration as a function of rock composition (Fig. 8b).

376 **3.7 Time Dependent Concentration Changes – Justification of Clay Stabilization through**
377 **exchange**

378   The trends in dissolved species concentration changes with time observed in the batch

379   reactor experiments provide clues on the stabilization of clay, but do not explain the high

380   concentration of other elements generally not associated with clay. In the time-dependent

381   analyses of various elemental concentrations presented in this section, we identify trends that

382   reveal that the most critical activity helping to stabilize clay minerals is cation exchange.

383   For all the reactions (Fig. 9), KCl solutions show a higher rate of dissolved species

384   concentration increase with time as well as larger changes in the rate, compared to DI water and

385 $C_5H_{14}ClNO$. Cationic concentrations and trends in $C_5H_{14}ClNO$ are marginally higher than in DI

386 water. The shift in trends over the experimental period is attributed to cation exchanges between

387 the clay components of rock and the fluids. The presence or absence of exchangeable cations in

388 the fluid is the main condition that may cause released ions in solution to remain or be consumed

389 in cation exchange processes. In KCl fluid, the presence of potassium cations, which easily

390 exchange for the exchangeable cations in the clay surfaces and interlayers, leaves more released

391 ions from the dissolution of calcite, dolomite, and silica polymorphs in solution.

392   The most favorable cation in the interlayer of illite clays is the potassium cation. In the

393 case of sodium and calcium cations released into KCl fluid, the potassium cations from KCl are

394 more favored to act at the cation exchange sites of clays, leaving sodium and calcium in solution.

395 In the case of DI water and $C_5H_{14}ClNO$, excess released sodium and calcium ions in solution are

396 adsorbed or exchanged at exchange sites of clay minerals.

397   It is also observed that, for anionic components like SO_4^{2-}, concentration trends with time

398 in all fluids are similar. This is because the concentration of SO_4^{2-} in solution is not dependent on

399 cationic exchange but likely due to dissolution of sulfide -bearing minerals such as pyrite

400 followed by oxidation. The consumption of ions by precipitation is observed to be the main

401 process by which anion concentrations in the sample are reduced. Therefore, SO_4^{2-} concentration

402 follows this trend.

403 **3.8 CT Scan and XRF analyses**

404   CT scan and XRF analyses were undertaken for the entire core run (650ft). Results from

405 these analyses are presented in Fig. 10. The CT images highlight gray-scale variations between

406 lithologic facies and XRF shows elemental distribution of various elements at different depths.

407 These are used to aid in predicting lithofacies and mineralogical composition of the formation

408 rock at the specific depth. Magnesium and potassium are missing from the chart because they fell

409 below the detection limit of the handheld XRF (2%). Average concentrations of Si, Al, Ca, S,

410 and Fe are 25.7%, 4.4%, 4.3%, 7989 ppm, and 19738 ppm, respectively.

411   Lithofacies based on the XRF was generated to denote zones in the well and to determine

412 their relationship with total organic carbon (TOC). This was done using classifications and

413 cutoffs [28] derived from Carmichaels, 1988. In this method, it is assumed that clay/shale portions

414 of the rock are represented by Al + Fe, carbonate facies are represented by Ca + Mg, and Si

14

415 represents Si rich rocks. For this well, cutoffs were adjusted to represent clay "rich", clay "lean",
416 and carbonates, based on the following discrete cutoffs: a clay cutoff of 22% was used to separate
417 clay "rich" facies from clay "lean" (Si-rich) and carbonate facies, and a quartz/carbonate ratio
418 (QC ratio) cutoff of 0.3 was used to separate carbonate from clay "lean" facies (Fig. 11). Fig. 11
419 shows a cross-plot of Si versus Al, with these facies identified, and Fig. 12 shows the resulting
420 XRF lithofacies for the cored section.

421   To explore the presence of non-detrital Si, Si versus Al, a cross-plot and Si/Al trends
422 were plotted to show a deviation from the normal detrital mode of sedimentation (Fig. 13). In the
423 case of the cross plot the red line indicates areas in the well where sedimentation is more clay
424 "rich" and data deviating from the line are likely deposited via biogenic Si or via eolian
425 processes. TOC data was added to the z-axis in Fig. 11, further denoting the possible presence of
426 biogenic Si.

427   Based on the elemental compositional plot from XRF (Fig. 10) and the XRF lithofacies
428 (Fig. 12), three key zones are identified within the investigated length of the core. These are
429 designated Upper, Middle, and Lower Caney (Fig. 10). The Upper Caney is characterized by
430 relatively high bioturbation with Si concentrations low within this zone. Si concentration is about
431 20% in clay rich (increased concentration of Al and Fe) zones and as low as 2% in carbonate rich
432 zones. Sulfur concentrations remain relatively constant throughout the Upper Caney. This zone is
433 thus predicted to be clay and carbonate-rich. The Middle Caney is characterized by almost
434 constant concentrations of Si and Al, approximately 28% and 8%, respectively. Ca concentration
435 in this section is low while there are slight increments in concentrations of Fe and S. This zone is
436 thus designated a Si-rich (i.e., clay lean) shale zone. Upper portions of the Lower Caney are
437 relatively carbonate rich considering the spike in Ca concentration with accompanying decline in
438 Si and Al concentrations. The remaining part of the Lower Caney however reverts to elemental
439 concentrations similar to the Upper Caney with intermittent carbonate-rich intervals. Fe in this
440 zone remains relatively constant. This zone is thus classified an interlayered carbonate- and Si-
441 rich zone. Results from XRF and classification of various zones coupled with results from batch
442 experiments are helpful in characterizing reactions and products when the formation interacts
443 with fracturing fluids.

444 **3.9 Numerical Model Results**

15

445   Results of Model 1 and Model 2 for aqueous species for the HC case in KCl solution are

446   shown in Figs. 14 and 15. The modeled pH at the experimental temperature was corrected by

447   numerically cooling the 95 °C samples to 25 °C while equilibrating them with atmospheric CO_2

448   (and not allowing mineral precipitation). The geochemical simulations also yield amounts of

449   minerals dissolved and of secondary phases formed (not shown). In Model 1, gibbsite is

450   modeled to eventually form as clays dissolve, which tends to depress the dissolved Al

451   concentration. In Model 2, gibbsite also forms but to a larger extent, depressing further the Al

452   concentrations; in addition, goethite forms as a result of pyrite oxidation, which is not considered

453   in Model 1 but is more representative of experimental conditions. Other potential secondary

454   phases included in the simulations (boehmite, siderite, and goethite) are not predicted to form in

455   either model.

456   **4.0 Discussion**

457   **4.1 Geochemical Reactions and their Impacts on wellbore production**

458   Clay minerals and non-clay minerals (carbonates and quartz) within a formation are

459   susceptible to geochemical interactions in the presence of fracturing fluids. Most shale

460   formations were deposited in sea water-rich environments and have established equilibrium of

461   their minerals and fluids over geological time. Once these formations are exposed to engineering

462   fluids, especially water-based fluids, the geochemical equilibrium established over geological

463   time is disturbed and this leads to chemical reactions [29]. High temperature and pressure

464   conditions in the subsurface, coupled with disturbed pH conditions enhance the chemical

465   reactions between hydraulic fracturing fluids and formation. The trends in elemental

466   concentrations in effluents from experiments show destabilization, dissolution and precipitation

467   patterns that are all meant to re-equilibrate the formation rock and fluids. Bratcher et al (2021)

468   showed that, reactions of carbonates are dependent on acidity of fracturing fluid whilst reaction

469   with aluminosilicates depended on the ionic strength of the fluid [30]. Dissolution of both species

470   are observed in our experiment, however, the scope of this work does not involve delineating the

471   impact of acidity and ionic strength. Future consideration of this will be important to clarify the

472   levels of acidity and ionic strength best suited for Caney shale fracturing.

473   The trends observed have implications on porosity and permeability of a reservoir. The

474   breakdown of clay minerals may cause migration of clay fines which will be deposited in flow

16

475 paths, whilst precipitation of new minerals can also form scales as well as grow to occlude flow

476 paths thus reducing the permeability of formation.

477 **4.2 Dissolution and Precipitation of Minerals**

478 Dissolution and precipitation of minerals result from interactions between the formation

479 rock minerals and engineered fluids, when the latter comes into contact with formation and

480 causes disequilibrium for hitherto stable minerals. For hydraulic fracturing and stimulation

481 operations, dissolution of rock forming minerals have been reported primarily for low pH

482 engineered fluids. As pH increases, ions from dissolved minerals contribute to formation of new

483 minerals and/or amorphous precipitates that may have an adverse effect on formation

484 permeability. In addition, such compositional alterations can impact mechanical properties of the

485 rock, contributing to increased proppant embedment and consequently reduction in fracture

486 network permeability. Geochemical reactivity of scale-forming minerals under these conditions

487 often result in reduced porosity and fracture permeability due to mineral dissolution and

488 precipitation [31,32]. At very high pH, clay minerals within a formation become unstable and may

489 become mobile. This situation leads to migration of illite samples which may occlude the

490 hydrocarbon flow paths within the formation. In our experiments, we observe almost all the

491 above reactions and more importantly continuous increase in pH, thus making the Caney Shale a

492 candidate for fines migration and scale formation. These are mostly responsible for deteriorating

493 productivities of formations in the long-term.

494 **4.3 Clays Interactions with Hydraulic Fracturing Fluids**

495 Water based fluids are highly reactive with clay minerals in the formation due to the polar

496 nature of water. Clay minerals also show high reactivity with fluids due to their charged surfaces.

497 The combination of these two characteristics provides a window of an extensive clays-fluids

498 interaction with significant implications on reservoir properties. These interactions lead to

499 dissolution, fines transport and/or clay swelling, which all alter the microstructure of the

500 formation rock [33,34]. Dissolution and ion exchange during fluid interactions with clay minerals

501 often leads to elevated elemental concentrations in subsurface fluids. With elemental

502 concentrations high, precipitation of new minerals occurs and these may occlude fractures

503 created by hydraulic fracturing, thus render the fracturing job unsuccessful. In this study, it was

504 observed that 2% KCl stabilized clays and increased the dissolution rates of carbonates.

17

4.4 Carbonates Interactions with Hydraulic Fracturing Fluids

Carbonate minerals react with hydraulic fracturing fluid under very low pH conditions leading to dissolution and precipitation of new minerals. The starting pH of 4 for KCl and $C_5H_{14}ClNO$ for experiments in this study caused initially high dissolution of carbonates. Dissolution of carbonates releases mainly Ca and Mg cations into solution. These cations may precipitate in the presence of high SO_4^{2-} concentrations in solution to form scales within the fracture walls thus reducing permeability of the formation. This observation has significant implications in the field conditions, especially in carbonate rich layers present in Caney Shale.

4.5 Pyrite Interactions with Hydraulic Fracturing Fluids

Pyrite is one of the main sources of SO_4^{2-} ions in fluids by oxidation of sulfide following interaction with hydraulic fracturing fluids. Dissolved oxygen in fracturing fluids has been identified as the main trigger responsible for pyrite dissolution. Dissolution of pyrite causes a pH decrease in fluids which may lead to increased dissolution of clays and mobilization of heavy metals [35]. The oxidation of Fe^{2+} to Fe^{3+} and sulfur to sulfate are the main ionic species produced from pyrite oxidative dissolution. These species mostly react with other ions in solution to form precipitates which may be responsible for occlusion of fractures. Though many researchers believe that salinity of fracturing fluids has an impact on pyrite dissolution, they consider this impact insignificant [36].

4.6 Quartz and Silica Interaction with Hydraulic Fracturing Fluids

Quartz dissolution due to interaction with fracturing fluid has been reported in most studies as being insignificant. This is due to the high stability of quartz. In this study, quartz is observed to be relatively stable. The dissolved silica reported in our experiments is presumed to result primarily from the dissolution of other more soluble and reactive forms of silica (such as opal-CT and amorphous silica, possibly of biogenic origin), possibly augmented by feldspar dissolution, and from desorption from clay mineral sites.

4.7 Preliminary Geochemical Modeling of Experiments

Agreement between both models and experiment for pH is reasonable (Figs. 14a,d), with pH mostly buffered by the carbonate content of the samples. The slightly lower simulated pH in Model 2, compared to Model 1, results from the oxidation of pyrite and carbon by O_2 introduced during sampling events (see further below).

18

535 The simulated Si concentration in Model 1 is much lower than observed values (Figs.
536 14b,e), thus cannot be explained by the dissolution of quartz and aluminosilicate minerals.
537 Observed dissolved Si concentrations could only be reached by including a more soluble SiO_2
538 polymorph in Model 2. Best results were obtained including about 5 vol.% opal CT as part of the
539 shale mineral assemblage (amorphous or small amounts of poorly crystalized SiO_2 polymorphs
540 such as opal would not be detected by XRD). This suggests that the shale contains other silica
541 polymorphs more soluble than quartz.

542 The simulated Ca concentration in Model 2 matches more closely the observed trend than
543 in Model 1 (Figs. 14c,f). The observed Ca concentrations could only be reproduced with Model
544 2 (Fig. 14f) by allowing the oxidation of small amounts of carbon (proxy for kerogen) and pyrite
545 during sampling events, causing the pH to be lower and subsequent more calcite dissolution than
546 with Model 1. To achieve these results, the O_2 concentration in air drawn into the beaker during
547 sampling was calibrated (~ 400 ppm) to match the calcium trend. It is noted that high (e.g.,
548 atmospheric) O_2 concentrations resulted in too much oxidation and pH decrease (and calcite
549 dissolution), suggesting that only minor oxidation occurred in the experiments. The dissolution
550 of plagioclase (Ca-feldspar) was also tested but could not produce enough calcium to match the
551 experimental data.

552 The observed Mg concentrations are also better matched with Model 2 (Figs. 15a,d),
553 which resulted in more chlorite precipitation (and subsequent Mg drop) than with Model 1
554 because of decreased grain size (thus faster reaction rate). Modeling the precipitation of other
555 clay minerals could not reproduce experimental results as well as chlorite precipitation. The low
556 levels of Al observed in the experiments (Figs. 15b,e) likely occur because Al drops out of
557 solution when the samples are cooled and filtered, and by the formation of secondary Al
558 hydroxide minerals such as gibbsite suggested by the simulations.

559 The observed rise in sodium concentrations (Figs. 15c,f) could not be reproduced, and
560 model results were found to be relatively insensitive to cation exchange capacity and exchange
561 constants. Observed Fe concentrations are essentially undetected and are computed (not shown)
562 to remains small with both Model 1 (in which essentially no pyrite dissolves) and Model 2 (in
563 which pyrite is oxidized and Fe drops out of solution a goethite). The oxidation of pyrite in

564 Model 2 causes an increase in modeled S concentration consistent with experimental results,
565 although reaching values only about half those observed (not shown).

566 It should be noted that model results are subject to large model input parameter
567 uncertainties, and similarly the experimental data is likely affected by experimental and
568 analytical error, together with uncertainties in redox conditions and possibly natural variations in
569 clay sample mineralogy and composition.

570 **5.0 Conclusions**

571 Predicted mineralogical compositions at various depths based on data obtained from
572 chemical compositional analyses by XRF also provide an understanding of the implications of
573 rock-fluid interactions on a larger scale (reservoir-scale) observed in batch experiments. The
574 following conclusions are therefore made from our experiments, models and analyses:

575 • pH buffering is significant for all rock types. The pH witnessed a significant recovery
576   following commencement of reactions, especially for KCl and $C_5H_{14}ClNO$ fluids which
577   were set to pH of 4 initially. This is believed to be the result of quick and significant
578   dissolution of carbonates. Lower pH triggered high dissolution rates for the rocks and as
579   pH increased, the rate of dissolution declined significantly, though for most cases
580   dissolution still continued.

581 • Observed dissolved Si concentrations were much higher than the quartz solubility,
582   suggesting that much of the Si originates from silica polymorphs more soluble than
583   quartz and desorption from clay mineral exchange sites.

584 • KCl fluid was effective in stabilizing clay minerals. This was mainly achieved through
585   cation exchanges between the fluid cations and cations located at exchange sites of clay
586   minerals. The potassium cation acts to significantly stabilize the clay (illite). $C_5H_{14}ClNO$
587   and DI water fluids were less effective in stabilizing the clay minerals.

588 • The amount of clay mineral composition has an inverse relationship with dissolution of
589   other minerals such as quartz, carbonates and pyrites. This may be due to the fact that
590   clay minerals typically form a matrix in which grains of carbonate, pyrite, and quartz are
591   imbedded thus clay reaction with fluids is predominant over these grains. The surface
592   area of clay may also explain its predominance in interacting with fluid first.

20

- Rapid decline of Al and Mg elemental concentrations are yet to be fully characterized and will be addressed in subsequent experiments. Two schools of thought exist for this behavior: Precipitation of Al- and Mg-bearing minerals, or rapid exchange and adsorption onto clay surfaces and interlayers.

- In general, preliminary geochemical modeling investigations (Model 2) support the conclusions regarding mineral dissolution and precipitation reached from experimental observations, notably the dissolution of calcite and oxidation of pyrite in reacted shale samples, the likely presence of silica polymorphs such as opal, chalcedony or amorphous silica in these samples, and the depression of Al and Mg concentrations in solution by precipitation of secondary aluminosilicate phases.

- Based on an integration of implications of all results obtained from experiments and modelling, post-fracturing geochemical reactions portends two major adverse outcomes; clay fines migration and precipitation of new minerals in flow paths. These both have negative impacts on long term permeability of the reservoir. It is however certain from our study that KCl clay stabilizer will effectively prevent clay platelet de-flocculation and clay fines migration.

References

(1) Radonjic, M.; Luo, G.; Wang, Y.; Achang, M.; Cains, J.; Katende, A.; Puckette, J.; Grammer, M.; King, G. E. Integrated Microstructural Characterisation of Caney Shale, OK. In *Unconventional Resources Technology Conference*; Austin, Texas, 2020; pp 1–18. https://doi.org/10.15530/urtec-2020-2947.

21

620 (2) Katende, A.; Rutqvist, J.; Benge, M.; Seyedolali, A.; Bunger, A.; Puckette, J. O.; Rhin, A.;
621   Radonjic, M. Convergence of Micro-Geochemistry and Micro-Geomechanics towards
622   Understanding Proppant Shale Rock Interaction: A Caney Shale Case Study in Southern
623   Oklahoma, USA. *J. Nat. Gas Sci. Eng.* **2021**, *96*, 104296.
624   https://doi.org/10.1016/j.jngse.2021.104296.

625 (3) Wang, Y.; Luo, G.; Achang, M.; Cains, J.; Wethington, C.; Katende, A.; Grammer, G. M.;
626   Puckette, J.; Pashin, J.; Castagna, M.; Chan, H.; King, G. E.; Radonjic, M. Multiscale
627   Characterization of the Caney Shale — An Emerging Play in Oklahoma. *Midcont. Geosci.*
628   **2021**, *2*, 33–53. https://doi.org/10.17161/mg.v2i.15911.

629 (4) Benge, M.; Lu, Y.; Katende, A.; Rutqvist, J.; Crandall, D.; Haecker, A.; King, G.; Renk, J.
630   B.; Radonjic, M.; Bunger, A. Connecting Geomechanical Properties with Potential for
631   Proppant Embedment and Production Decline for the Emerging Caney Shale, Oklahoma;
632   OnePetro, 2021. https://doi.org/10.15530/urtec-2021-5084.

633 (5) Awejori, G. A.; Radonjic, M. Review of Geochemical and Geo-Mechanical Impact of
634   Clay-Fluid Interactions Relevant to Hydraulic Fracturing. In *Hydraulic Fracturing*;
635   Kenneth Imo-Imo Israel Eshiet, Ed.; IntechOpen, 2021.
636   https://doi.org/10.5772/INTECHOPEN.98881.

637 (6) Cardott, B. J. Oklahoma Shale Resource Plays. *Okahoma Geol. Notes* **2017**, No. April-
638   June, 21–30.

639 (7) Haluszczak, L. O.; Rose, A. W.; Kump, L. R. Geochemical Evaluation of Flowback Brine
640   from Marcellus Gas Wells in Pennsylvania, USA. *Appl. Geochem.* **2013**, *28*, 55–61.
641   https://doi.org/10.1016/J.APGEOCHEM.2012.10.002.

642 (8) Chen, H.; Carter, K. E. Characterization of the Chemicals Used in Hydraulic Fracturing
643   Fluids for Wells Located in the Marcellus Shale Play. *J. Environ. Manage.* **2017**, *200*,
644   312–324. https://doi.org/10.1016/J.JENVMAN.2017.05.069.

645 (9) Harrison, A. L.; Jew, A. D.; Dustin, M. K.; Thomas, D. L.; Joe-Wong, C. M.; Bargar, J.
646   R.; Johnson, N.; Brown, G. E.; Maher, K. Element Release and Reaction-Induced Porosity
647   Alteration during Shale-Hydraulic Fracturing Fluid Interactions. *Appl. Geochem.* **2017**,
648   *82*, 47–62. https://doi.org/10.1016/J.APGEOCHEM.2017.05.001.

649 (10) Zeng, L.; Lu, Y.; Al Maskari, N. S.; Chen, Y.; Hossain, M. M.; Saeedi, A.; Dautriat, J.;

22

Xie, Q. Interpreting Micromechanics of Fluid-Shale Interactions with Geochemical Modelling and Disjoining Pressure: Implications for Calcite-Rich and Quartz-Rich Shales. *J. Mol. Liq.* **2020**, *319*, 114117. https://doi.org/10.1016/J.MOLLIQ.2020.114117.

(11) Olabode, A.; Bentley, L.; Radonjic, M. Shale Caprock Integrity under Carbon Sequestration Conditions. *AIP Conf. Proc.* **2012**, *1453* (1), 347. https://doi.org/10.1063/1.4711198.

(12) Olabode, A.; Radonjic, M. Geochemical Markers in Shale-CO2 Experiment at Core Scale. *Energy Procedia* **2017**, *114*, 3840–3854. https://doi.org/10.1016/J.EGYPRO.2017.03.1516.

(13) Wang, W.; Wei, W. Water Chemistry. In *Fluid Chemistry, Drilling and Completion*; Elsevier, 2022; pp 95–114. https://doi.org/10.1016/B978-0-12-822721-3.00005-8.

(14) Salles, F.; Beurroies, I.; Bildstein, O.; Jullien, M.; Raynal, J.; Denoyel, R.; Damme, H. Van. A Calorimetric Study of Mesoscopic Swelling and Hydration Sequence in Solid Na-Montmorillonite. *Appl. Clay Sci.* **2008**, *39* (3–4), 186–201. https://doi.org/10.1016/j.clay.2007.06.001.

(15) Doostmohammadi, R.; Moosavi, M. Swelling of Weak Rocks, Effective Parameters and Controlling Methods. In *ISRM International Symposium - 5th Asian Rock Mechanics Symposium 2008, ARMS 2008*; 2008; pp 247–253.

(16) Botan, A.; Rotenberg, B.; Marry, V.; Turq, P.; Noetinger, B. Carbon Dioxide in Montmorillonite Clay Hydrates: Thermodynamics, Structure, and Transport from Molecular Simulation. *J. Phys. Chem. C* **2010**, *114* (35), 14962–14969. https://doi.org/10.1021/jp1043305.

(17) Warr, L.; Berger, J. Hydration of Bentonite in Natural Waters: Application of "Confined Volume" Wet-Cell X-Ray Diffractometry. *Phys. Chem. Earth* **2007**, *32* (1–7), 247–258. https://doi.org/10.1016/j.pce.2006.02.048.

(18) Patel, A.; Stamatakis, E.; Young, S.; Friedheim, J. Advances in Inhibitive Water-Based Drilling Fluids - Can They Replace Oil-Based Muds? In *Proceedings - SPE International Symposium on Oilfield Chemistry*; OnePetro, 2007; pp 614–621. https://doi.org/10.2118/106476-ms.

(19) Bedrikovetsky, P.; Zeinijahromi, A.; Siqueira, F. D.; Furtado, C. A.; de Souza, A. L. S.

23

680   Particle Detachment Under Velocity Alternation During Suspension Transport in Porous

681   Media. *Transp. Porous Media* **2012**, *91* (1), 173–197. https://doi.org/10.1007/s11242-011-

682   9839-1.

683   (20) Knappett, J. A.; Craig, R. F. *Craig's Soil Mechanics, Eighth Edition*; Spon Press,:

684   Abingdon, Oxon ;;New York :, 2012. https://doi.org/10.1201/b12841.

685   (21) El-Monier, I. A.; Nasr-El-Din, H. A. Mitigation of Fines Migration Using a New Clay

686   Stabilizer: A Mechanistic Study. In *Society of Petroleum Engineers - 9th European*

687   *Formation   Damage   Conference   2011*;   2011;   Vol.   2,   pp   1162–1173.

688   https://doi.org/10.2118/144180-ms.

689   (22) Vidic, R. D.; Brantley, S. L.; Vandenbossche, J. M.; Yoxtheimer, D.; Abad, J. D. Impact

690   of Shale Gas Development on Regional Water Quality. *Science* **2013**, *340* (6134),

691   1235009. https://doi.org/10.1126/science.1235009.

692   (23) Paronish, T.; Schmitt, R.; Moore, J.; Crandall, D.; Rihn, A.; Renk, J.; Doughty, C.;

693   Bunger, A.; Wang, Y.; Katende, A.; Seyedolali, A.; Puckette, J.; Radonjic, M. *Computed*

694   *Tomography Scanning and Geophysical Measurements of the Caney Shale Formation*

695   *from the Tomaney #1-35-34-27 Well*; 2021. https://doi.org/10.2172/1812176.

696   (24) Paronish, T.; Mackey, P.; Crandall, D.; Moore, J.; Brown, S.; T., C.; Martin, K. Computed

697   Tomography Scanning and Geophysical Measurements of Core from the Marcellus Shale

698   Energy and Environment Laboratory. *Natl. Energy Technol. Lab.* **2018**, No. (Netl-Trs-22-

699   2018), 58. https://doi.org/10.18141/1488537.

700   (25) Xu, T.; Sonnenthal, E.; Spycher, N.; Zheng, L. *TOUGHREACT V3.0-OMP Reference*

701   *Manual: A Parallel Simulation Program for Non-Isothermal Multiphase Geochemical*

702   *Reactive Transport: V3-OMP Reference Manual Authors: Tianfu Xu, Eric Sonnenthal,*

703   *Nicolas Spycher, and Liange Zheng*; California, 2014.

704   (26) Xu, T.; Sonnenthal, E.; Spycher, N.; Zheng, L. *TOUGHREACT V3.0-OMP Sample*

705   *Problems: V3-OMP Sample Problem Authors: Tianfu Xu, Eric Sonnenthal, Nicolas*

706   *Spycher, and Liange Zheng Toughreact V3-OMP Code Authors*; California, 2014.

707   (27) Hingston, F. J. Reactions between Boron and Clays. *Soil Res.* **1964**, *2* (1), 83–95.

708   https://doi.org/10.1071/SR9640083.

709   (28) Carmichael, R. S. *Practical Handbook of Physical Properties of Rocks and Minerals*, 1st

24

710 ed.; Carmichael, R. S., Ed.; CRC Press Revivals, 1988.
711 https://doi.org/10.1201/9780203710968.

712 (29) Edgin, M. G.; Medina-Rodriguez, B.; Kaszuba, J. P.; Dewey, J. C.; Alvarado, V.
713 Geochemical Reactions and Alteration of Pore Architecture in Saturated Shale after
714 Injection of Stimulation Fluid. *Fuel* **2021**, *303*, 120815.
715 https://doi.org/10.1016/J.FUEL.2021.120815.

716 (30) Bratcher, J. C.; Kaszuba, J. P.; Herz-Thyhsen, R. J.; Dewey, J. C. Ionic Strength and PH
717 Effects on Water-Rock Interaction in an Unconventional Siliceous Reservoir: On the Use
718 of Formation Water in Hydraulic Fracturing. *Energy Fuels* **2021**, *35* (22), 18414–
719 18429.https://doi.org/10.1021/ACS.ENERGYFUELS.1C02322/ASSET/IMAGES/
720 MEDIUM/EF1C02322_M001.GIF.

721 (31) Ellis, B. R.; Fitts, J. P.; Bromhal, G. S.; McIntyre, D. L.; Tappero, R.; Peters, C. A.
722 Dissolution-Driven Permeability Reduction of a Fractured Carbonate Caprock. *Environ.*
723 *Eng. Sci.* **2013**, *30* (4), 187–193. https://doi.org/10.1089/ees.2012.0337.

724 (32) Nogues, J. P.; Fitts, J. P.; Celia, M. A.; Peters, C. A. Permeability Evolution Due to
725 Dissolution and Precipitation of Carbonates Using Reactive Transport Modeling in Pore
726 Networks. *Water Resour. Res.* **2013**, *49* (9), 6006–6021.
727 https://doi.org/10.1002/wrcr.20486.

728 (33) Liang, F.; Zhang, J.; Liu, H. H.; Bartko, K. M. Multiscale Experimental Studies on
729 Interactions between Aqueous-Based Fracturing Fluids and Tight Organic-Rich Carbonate
730 Source Rocks. In *SPE Reservoir Evaluation and Engineering*; 2019; Vol. 22, pp 402–417.
731 https://doi.org/10.2118/192411-PA.

732 (34) Marcon, V.; Joseph, C.; Carter, K. E.; Hedges, S. W.; Lopano, C. L.; Guthrie, G. D.;
733 Hakala, J. A. Experimental Insights into Geochemical Changes in Hydraulically Fractured
734 Marcellus Shale. *Appl. Geochem.* **2017**, *76*, 36–50.
735 https://doi.org/10.1016/j.apgeochem.2016.11.005.

736 (35) Pearce, J. K.; Turner, L.; Pandey, D. Experimental and Predicted Geochemical Shale-
737 Water Reactions: Roseneath and Murteree Shales of the Cooper Basin. *Int. J. Coal Geol.*
738 **2018**, *187*, 30–44. https://doi.org/10.1016/J.COAL.2017.12.008.

739 (36) Fazeli, H.; Vandeginste, V.; Rabbani, A.; Babaei, M.; Muljadi, B. Pore-Scale Modeling of

Fluid-Rock Chemical Interactions in Shale during Hydraulic Fracturing. *Energy Fuels* **2021**, *35* (13), 10461–10474.

Mineral	HQ	MQ	HC
Quartz	72	54.1	36.3
Albite		4.1	
Pyrite	2.5	4.8	5.2
Calcite	6.6	9	5.4
Dolomite	3	8.1	8.7
Illite	9.1	13.3	27.3
Illite/ Smectite	2.1	2.1	4.2
Muscovite	4.8	4.4	12.9

Table 1. Summary of mineralogical composition of rock samples.

Table 2. Summary of experimental fluid compositions.

26

Cases	Fluid Compositions
Case 1	DI water, pH ~7
Case 2	DI water, 2% KCl, pH ~4
Case 3	DI water, 0.5% Choline Chloride, pH ~4

760

761 **Table 3. Minerals considered in the TOUGHREACT simulations for the High Clay (HC)**
762 **sample.**

Primary Minerals:	Volume Fraction Model 1	Volume Fraction Model 2
Quartz	0.319	0.269
Maximum Microcline	0.013	0.013
Albite	0.037	0.037
Pyrite	0.063	0.063
Calcite	0.136	0.136
Dolomite	0.006	0.006
Montmorillonite-Ca	0.254	0.254
Illite	0.105	0.105
Kaolinite	0.056	0.056
Clinochlore-14A	0.011	0.011
Opal-CT	-	0.050
Carbon (graphite)	-	0.010

Secondary minerals allowed to form:
Kaolinite
Gibbsite
Boehmite
Siderite
Goethite

763

764
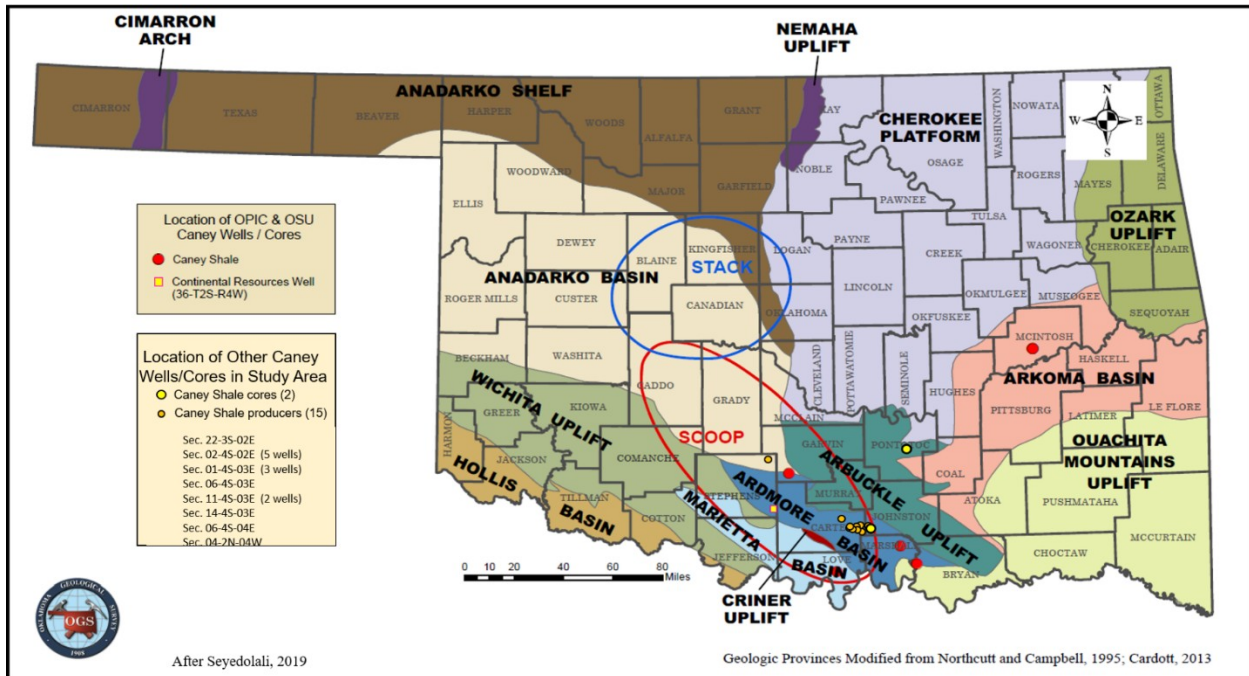
Fig. 1: Geological map of Oklahoma, showing SCOOP area (Red ellipsoid) and locations where Caney Wells were drilled (Red Dot within ellipsoid) (Modified from Cardott, 2013)

769

Arkoma Basin Stratigraphy				
Age	**Period**	**Epoch**		**Formation**
			Desmoinisian	Senora Formation
				Staurt Formation
				Thurman Formation
				Boggy formation
				Bluejacket Formation
				Savanna Formation
				McAlester Formation
				Hartshorne Formation
			Atokan	Atoka Formation
			Morrowan	Wepanucka Formation
			Chesterian	Springer Group/Union Valley Formation
			Meramecian	**Caney Shale**
			Osagean	
350Ma			Kinderhookian	
			Upper	Woodford Shale
			Middle	
410Ma			Lower	Hunton Group
	Silurian		Upper	
444Ma			Lower	
			Upper	Sylvan Shale
			Middle	Viola Group Simpson Group
485Ma			Lower	
541Ma	Cambrian		Upper	Arbuckle Group

770
771 Fig. 2: Stratigraphic Column showing Caney Shale position relative to other Formations in the Arkoma Basin.
772

29

773
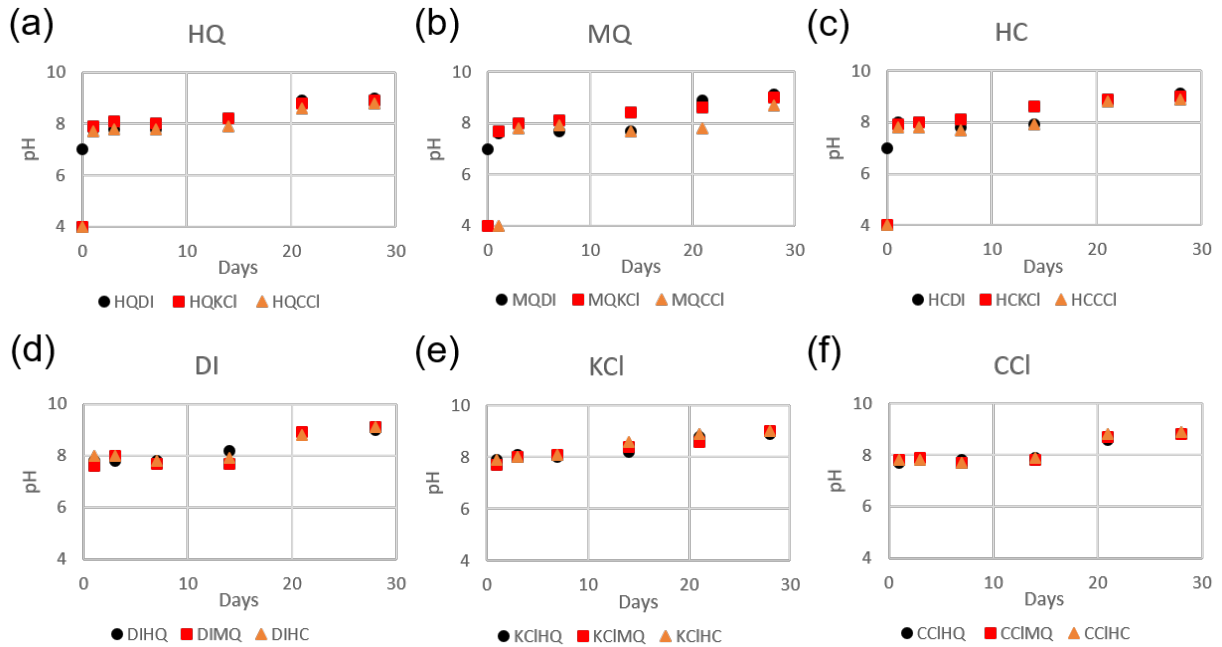
774 Fig. 3. (a-c) Variance of pH with time for different fluids: **left:** High Quartz (HQ). **middle:** Moderate Quartz

775 Carbonate and Clay (MQ). **right:** High Clay (HC). (d-f) Variance of pH with time for different rocks in different

776 water types: **left:** DI water (DI). **middle:** potassium chloride (KCl). **right:** choline chloride (CCl).
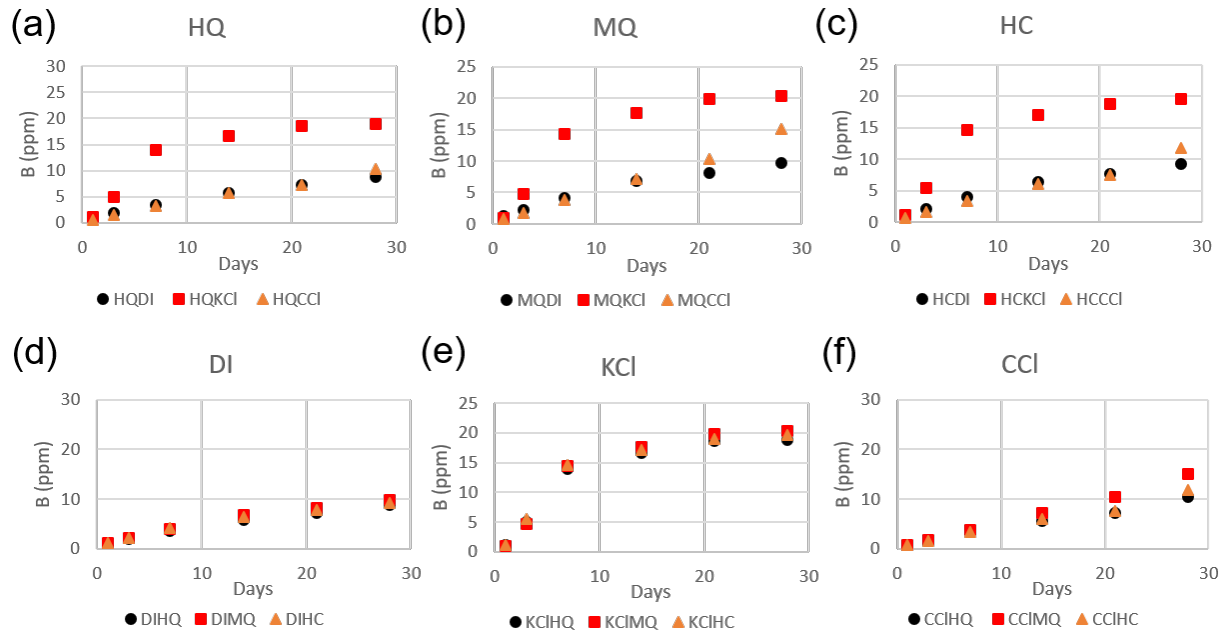
777

778
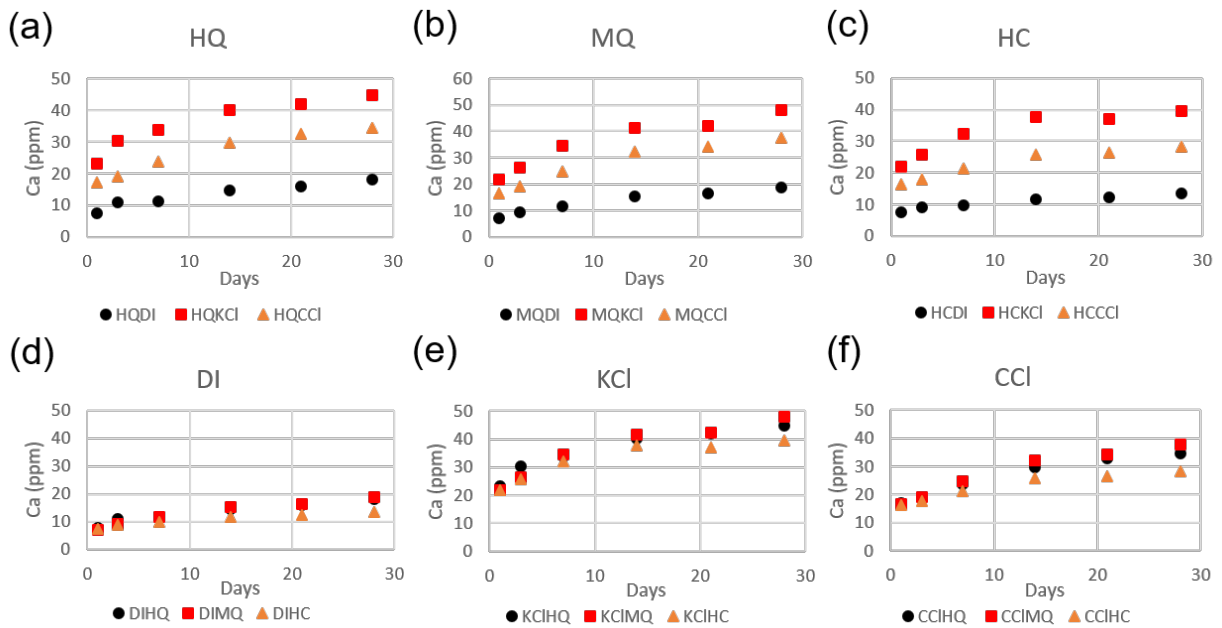
Fig. 4. (a-c) Variance of Ca concentration with time for different fluids: **left:** High Quartz (HQ). **middle:** Moderate

Quartz Carbonate and Clay (MQ). **right:** High Clay (HC). (d-f) Variance of Ca concentration with time for different

rocks in different water types: **left:** DI water (DI). **middle:** potassium chloride (KCl). **right:** choline chloride (CCl).
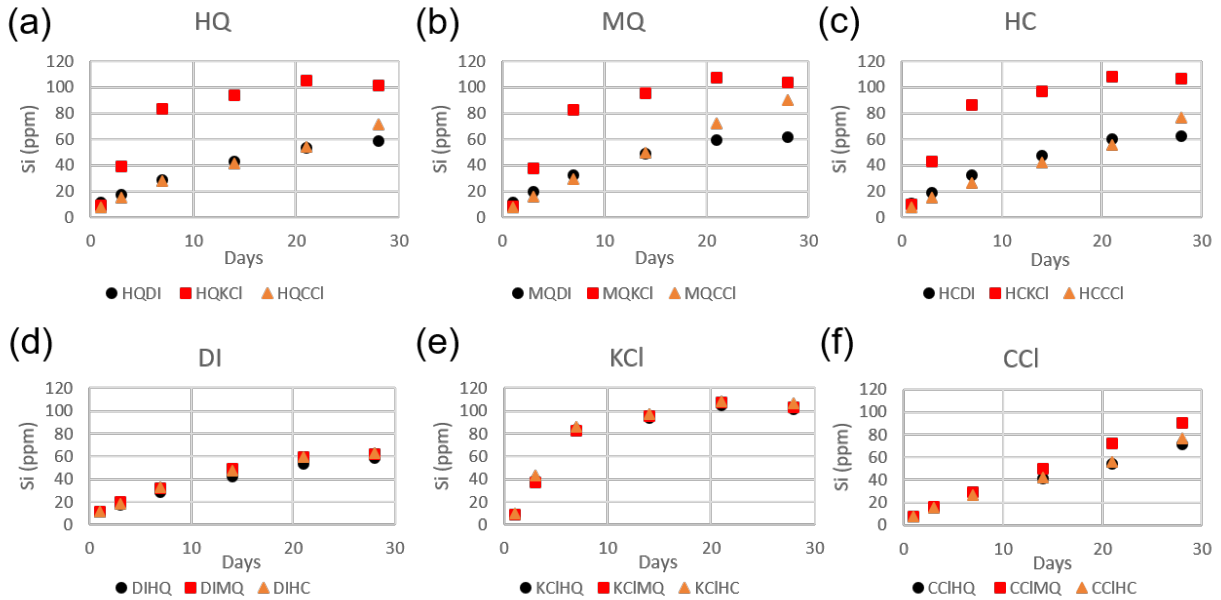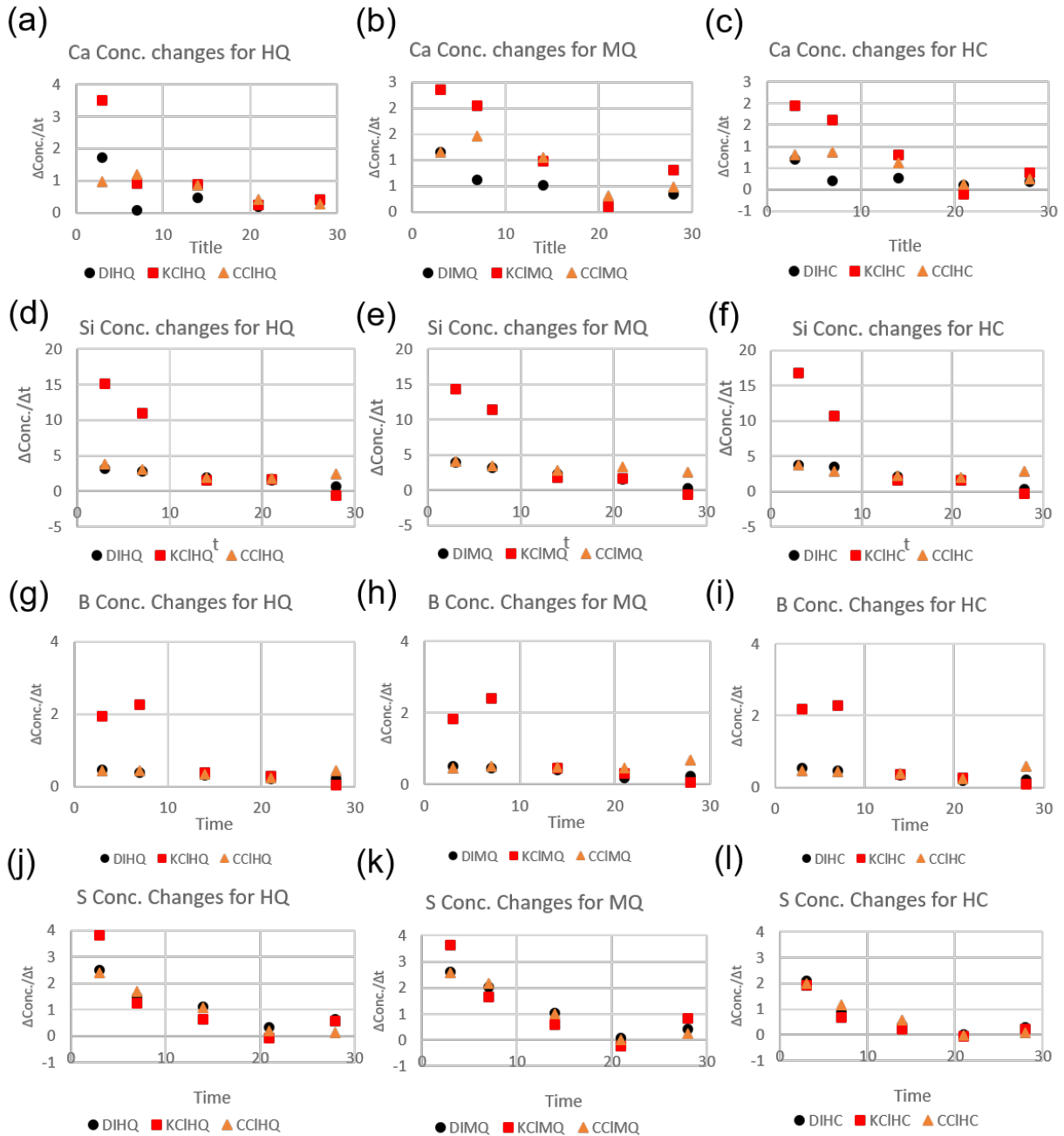

Fig. 5. (a-c) Variance of Si concentration with time for different fluids: **left:** High Quartz (HQ). **middle:** Moderate

Quartz Carbonate and Clay (MQ). **right:** High Clay (HC). (d-f) Variance of Si concentration with time for different

rocks in different water types: **left:** DI water (DI). **middle:** potassium chloride (KCl)**. right:** choline chloride (CCl).
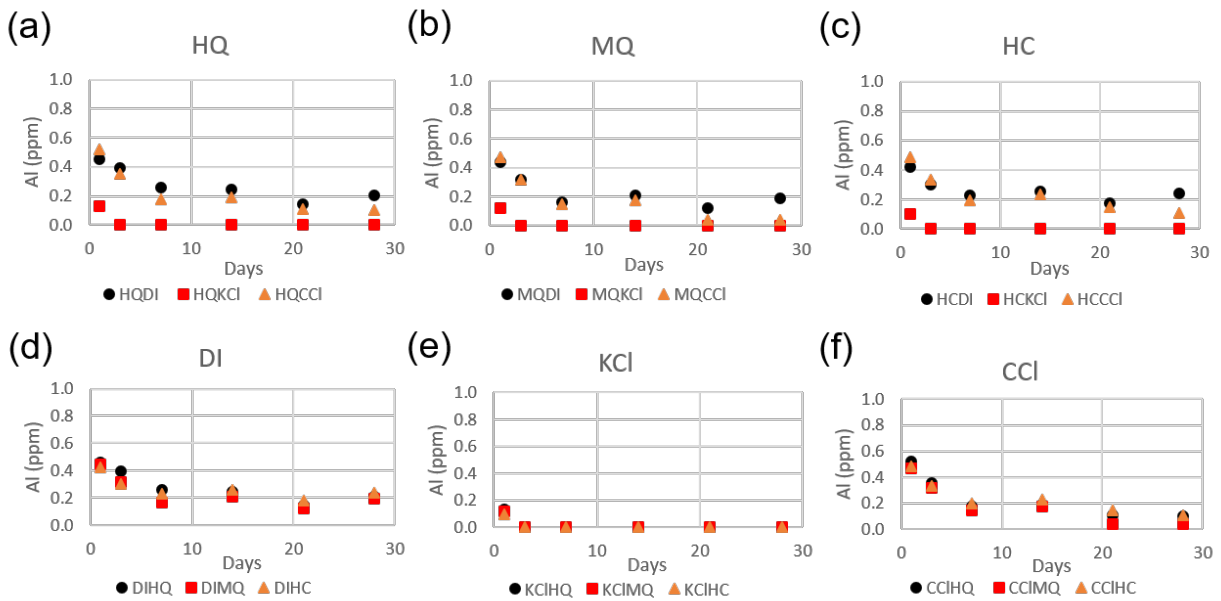
Fig. 6. (a-c) Variance of Al concentration with time for different fluids: **left:** High Quartz (HQ). **middle:** Moderate

789 Quartz Carbonate and Clay (MQ). **right:** High Clay (HC). (d-f) Variance of Al concentration with time for different

790 rocks in different water types: **left:** DI water (DI). **middle:** potassium chloride (KCl)**. right:** choline chloride (CCl).

791
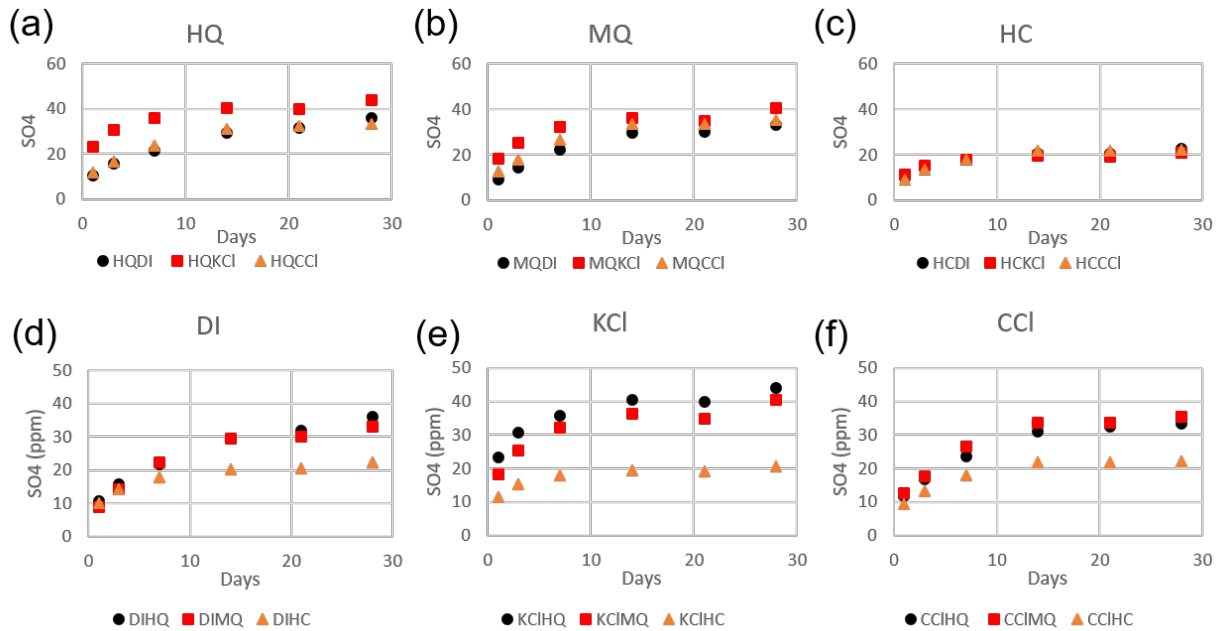
792

793 Fig. 7. (a-c) Variance of S concentration with time for different fluids: **left:** High Quartz (HQ). **middle:** Moderate

794 Quartz Carbonate and Clay (MQ). **right:** High Clay (HC). (d-f) Variance of S concentration with time for different

795 rocks in different water types: **left:** DI water (DI). **middle:** potassium chloride (KCl). **right:** choline chloride (CCl).

796

797

Fig. 8. (a-c) Variance of B concentration with time for different fluids: **left:** High Quartz (HQ). **middle:** Moderate

Quartz Carbonate and Clay (MQ)**. right:** High Clay (HC). (d-f) Variance of B concentration with time for different

rocks in different water types: **left:** DI water (DI). **middle:** potassium chloride (KCl). **right:** choline chloride (CCl).

801

Fig. 9. (a-c) Rate of Ca concentration change with time in fluids (DI, KCl, CCl) for different rock compositions: **left:** High Quartz (HQ). **middle:** Moderate Quartz Carbonate and Clay (MQ). **right:** High Clay (HC). (d-f) Rate of Si concentration change with time in fluids (DI, KCl, CCl) for different rock compositions in different water types: **left:** High Quartz (HQ). **middle:** Moderate Quartz Carbonate and Clay (MQ). **right:** High Clay (HC). (g-i) Rate of B concentration change with time in fluids (DI, KCl, CCl) for different rock compositions: **left:** High Quartz (HQ). **middle:** Moderate Quartz Carbonate and Clay (MQ). **right:** High Clay (HC). (j-l) Rate of S concentration change with time in the three fluids (DI, KCl, CCl) for different rock compositions: **left:** High Quartz (HQ). **middle:** Moderate Quartz Carbonate and Clay (MQ). **right:** High Clay (HC).

34

811
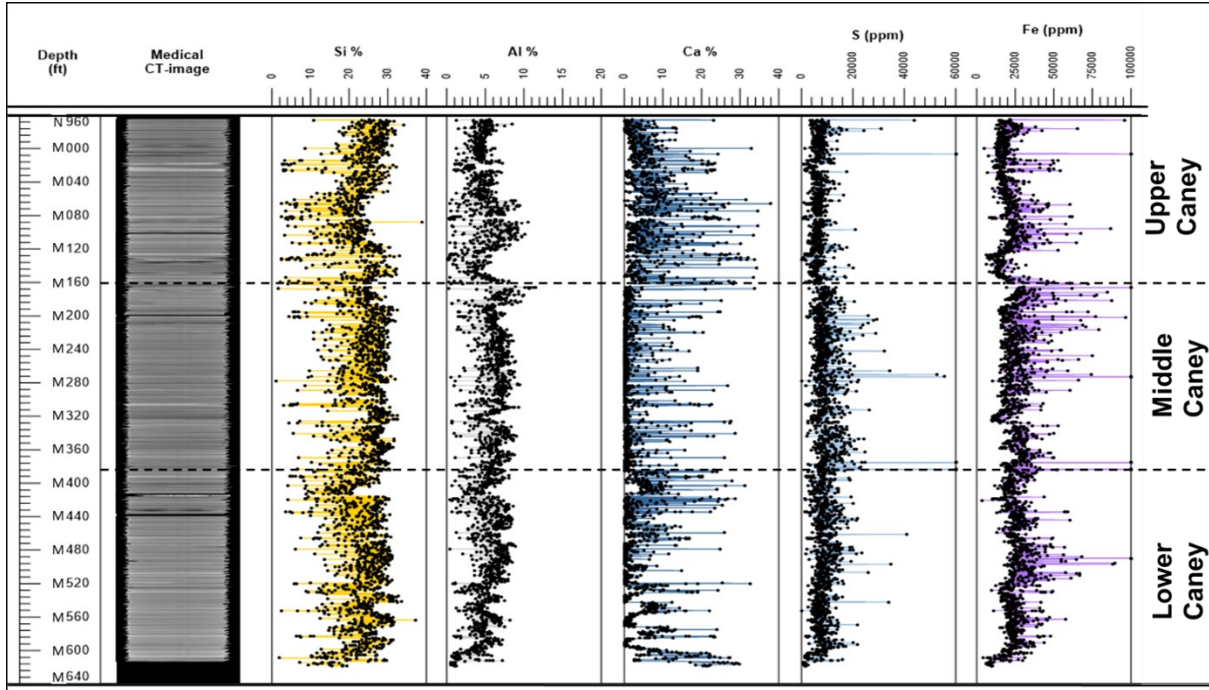
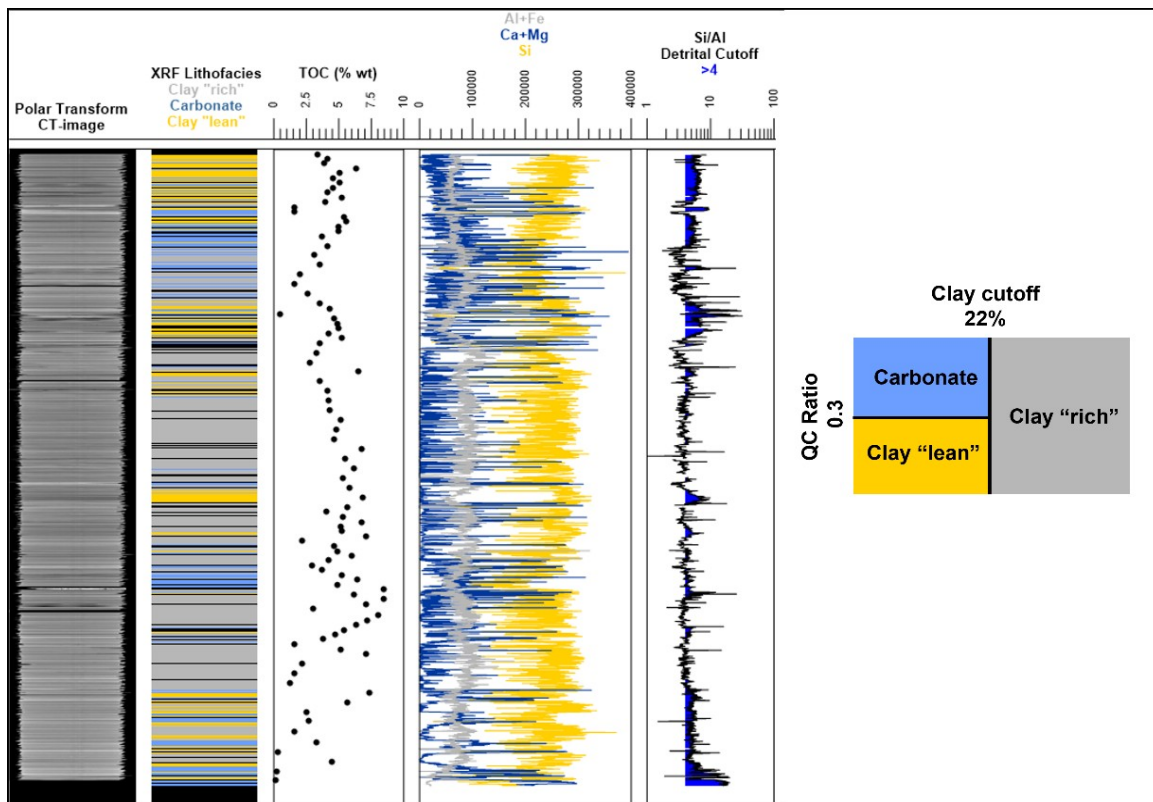Fig. 10. XRF elemental concentration graph for entire 650ft core retrieved from Caney Shale

814

815
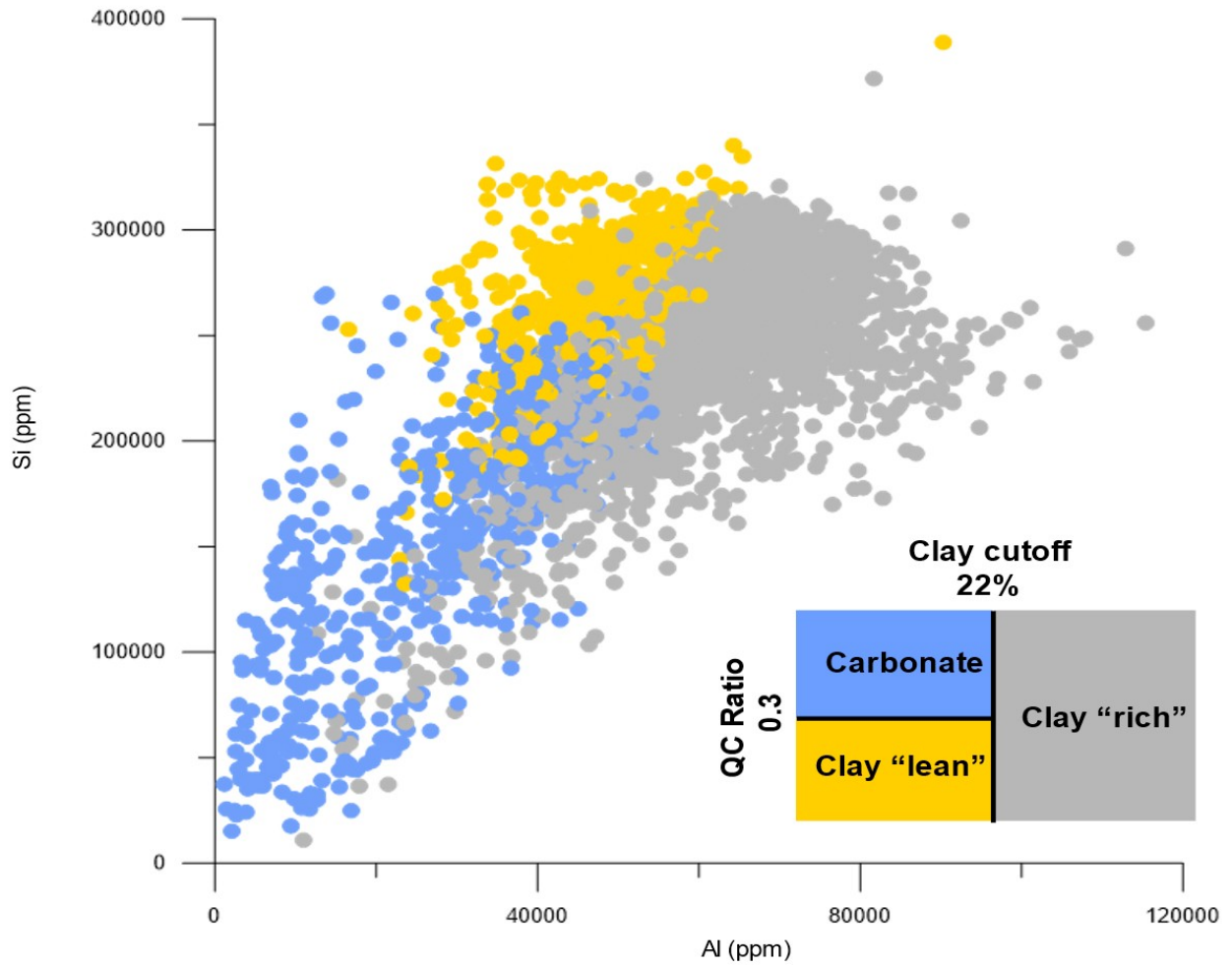
816
817 Fig. 11. Cross-plot of silica (quartz composition) versus aluminum (clay composition) based on results from XRF
818 measurements. Blue points are carbonates, gold points as clay lean, and gray points as clay rich.
819
820

821

822

823

824

825

826

827

828

829

36

830

831

Fig. 12. Corroboration of CT scan and XRF lithofacies generated using cutoffs on right side of figure as well as TOC, XRF components, Si/Al (with detrital cutoff of greater than 4 for biogenic and/or eolian Si).
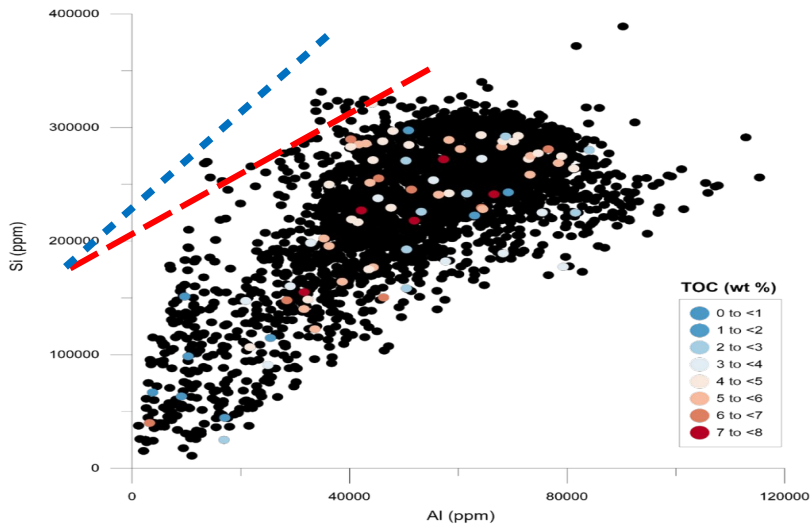
Fig. 13. Cross-plot of silicon (quartz composition) versus Al (clay composition) with the red line representing the
sedimentation line and the colored dots represent TOC (wt%), the blue line indicates the "clay" cutoff line.
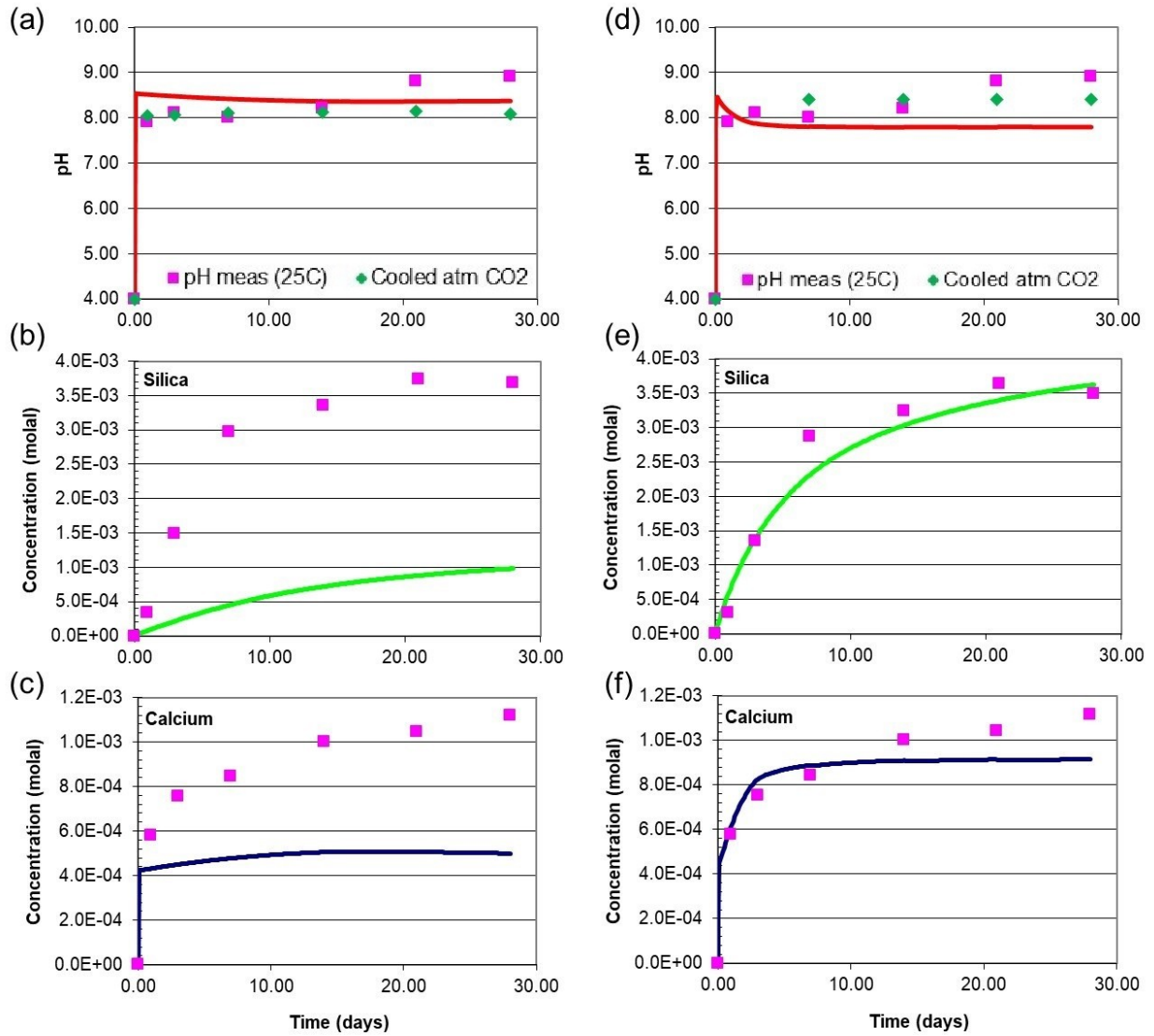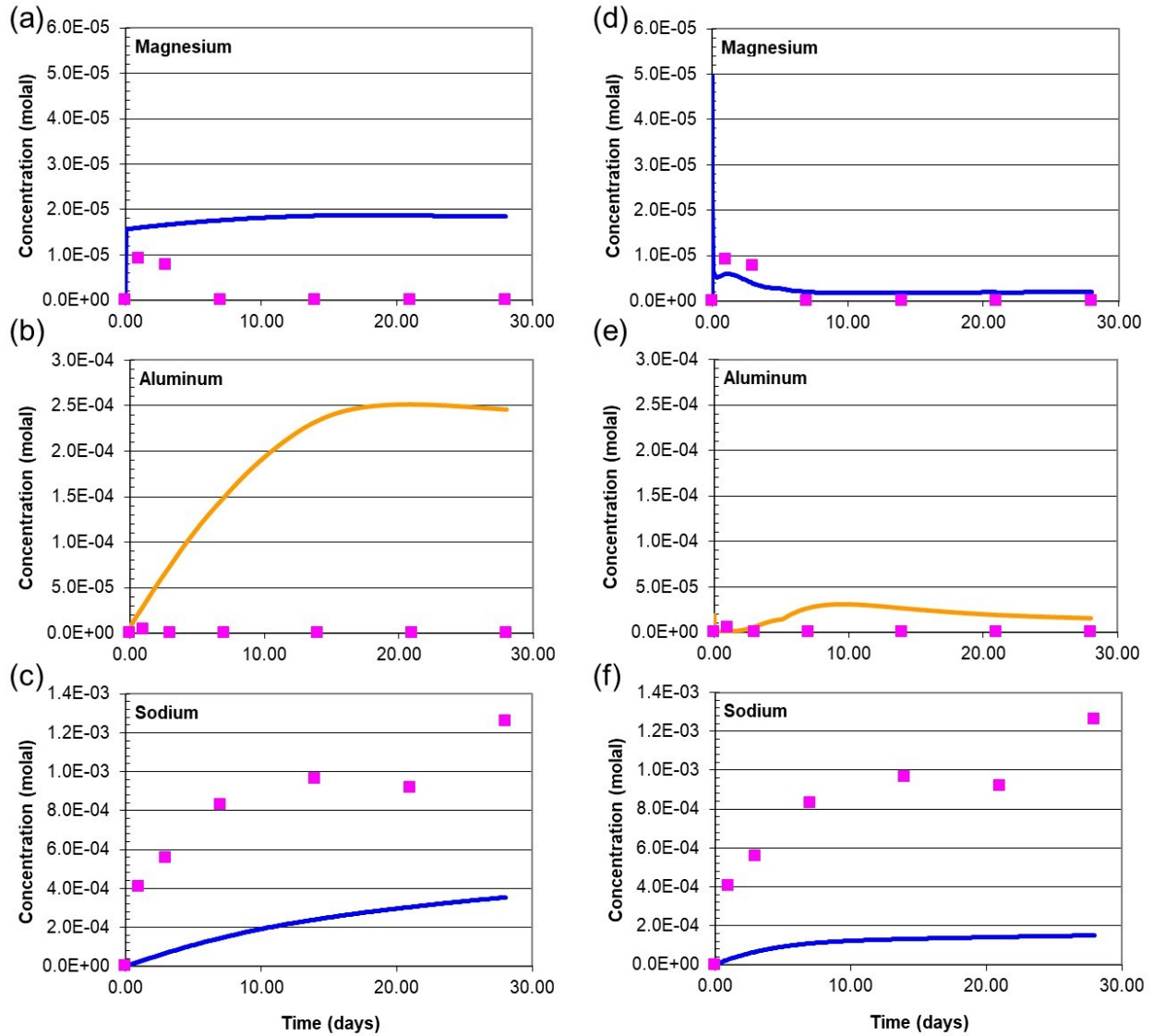
839

840   Fig. 14. Comparison of model (lines) and experimental (symbols) results for the High Clay (HC) case in

841   KCl solutions with Model 1 (a,b,c) and Model 2 (d,e,f) for pH, Si and Ca.

842

Fig. 15. Comparison of model (lines) and experimental (symbols) results for the High Clay (HC) case in KCl solutions with Model 1 (a,b,c) and Model 2 (d,e,f) for Mg, Al and Na.

843
844

845

846

847

848

849

850

40